Kent Academic Repository

Childers, Matthew Carter, Geeves, Michael A and Regnier, Michael (2024) *Interacting myosin head dynamics and their modification by 2'-deoxy-ADP*. **Biophysical journal . ISSN 0006-3495.**

Interacting myosin head dynamics and their modification by 2'-deoxy-ADP

Matthew Carter Childers[1], Michael A. Geeves[2] and Michael Regnier[1*]

1. Department of Bioengineering, School of Medicine, University of Washington, Seattle, WA, USA
2. Department of Biosciences, University of Kent, Canterbury, Kent CT2 7NJ, UK

Abstract

The contraction of striated muscle is driven by cycling myosin motor proteins embedded within the thick filaments of sarcomeres. In addition to cross-bridge cycling with actin, these myosin proteins can enter an inactive, sequestered state in which the globular S1 heads rest along the thick filament surface and are inhibited from performing motor activities. Structurally, this state is called the interacting heads motif (IHM) and is a critical conformational state of myosin that regulates muscle contractility and energy expenditure. Structural perturbation of the sequestered state can pathologically disrupt IHM structure and the mechanical performance of muscle tissue. Thus, the IHM state has become a target for therapeutic intervention. An ATP analogue called 2'-deoxy-ATP (dATP) is a potent myosin activator that destabilizes the IHM. Here, we use molecular dynamics simulations to study the molecular mechanisms by which dATP modifies the structure and dynamics of myosin in a sequestered state. Simulations of the IHM state containing ADP.Pi in both nucleotide binding pockets revealed dynamic motions of the blocked head – free head interface, light chain binding domain, and S2 in this 'inactive' state of myosin. Replacement of ADP.Pi by dADP.Pi triggered a series of structural changes that increased heterogeneity among residue contact pairs at the blocked head – free head interface and a 14% decrease in the interaction energy at the interface. Dynamic changes to this interface were accompanied by dynamics in the light chain binding region. A comparative analysis of these dynamics predicted new structural sites that may affect IHM stability.

Statement of Significance: Myosins, the ATP-driven motor proteins of muscle tissues, can adopt an inactive conformation called the interacting heads motif (IHM). In this conformation, myosin motors have low ATP consumption and cannot interact with actin filaments to generate force. Regulation of the IHM thus regulates muscle contractility. The objectives of this study are to understand the extent of conformational flexibility in the inactive state and to determine how stability may be reduced or disrupted by the myosin activator dATP. Here, we use molecular simulations to study IHM dynamics, predict the effects of an ATP analogue, and identify residues critical for regulating IHM stability.

Key Words:

Myosin motor, interacting heads motif (IHM), super-relaxed state (SRX), molecular dynamics, muscle regulation, muscle structure and function

Introduction

Within striated muscle sarcomeres, the myosin motors of the thick filament bind to the actin strands of thin filaments and give rise to contraction via cross-bridge cycling. (1, 2) In thick filaments, myosin motors form heterohexamers comprised of two myosin heavy chains (MHC), two essential light chains (ELC), and two regulatory light chains (RLC). (Figure 1A) Myosin heavy chains can be divided into the motor domain (Figure 1B) and a tail that adopts α-helical structure. The motor domain performs ATP hydrolysis, interacts with actin filaments, and triggers conformational changes associated with the powerstroke. The tail forms a coiled-coil structure (called S2) and tails of multiple myosins assemble with other proteins into thick filaments. The interacting heads motif (IHM) myosin state on the thick filament backbone forms as the actin binding region of the 'blocked head' (BH) motor domain (Figure 1A, orange) 'folds back' to interact with the 'free head' (FH) and coiled-coil S2 region (3). (Figure 1A, purple) This interaction is made possible through specific bending of hinges in the myosin light chain binding domain (LCBD) region of the tail. (4, 5)
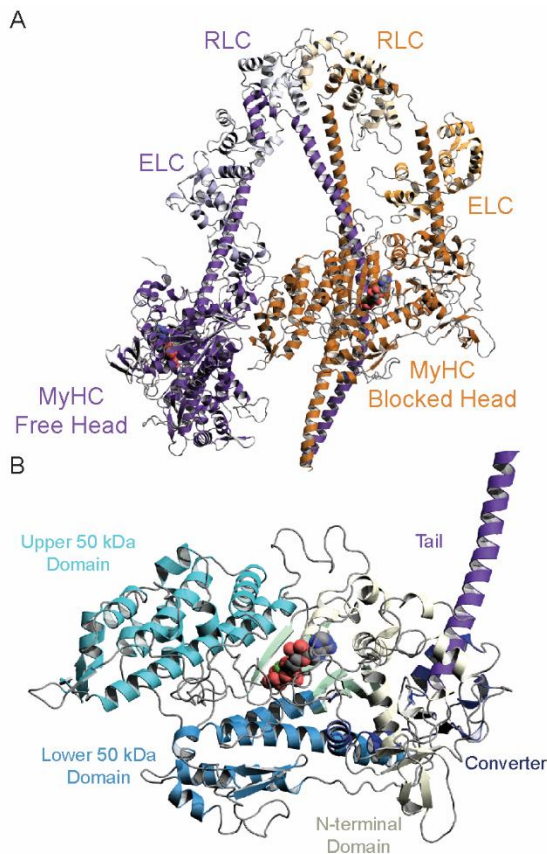

Figure 1. Schematic of the actin-myosin chemomechanical cycle. (A) We simulated a myosin IHM construct that contains a blocked head (orange) and free head (purple) along with their associated regulatory (RLC) and essential (ELC) light chains. Ligands (Mg^{2+}-(d)ADP.Pi) in the nucleotide binding pockets are shown as spheres. (B) The motor domain of myosin can be divided into four large domains: the upper (cyan) and lower (blue) 50 kDa domains form the actin ~~binding~~ and free head binding sites. The N-terminal domain (gold) and converter (dark blue) domain form a hinge site around which the tail (purple) rotates during the powerstroke.

In active muscle, contraction depends on concerted interactions and dynamic conformational changes within and between myosin motors and actin filaments (i.e. cross-bridges), in a process driven by ATP hydrolysis. (1) Contractile magnitude is the product of the number of cross-bridges and the rate of cross-bridge cycling. In addition to active, cycling conformations associated with actin binding and force generation (2), myosins can access inactive, non-cycling states with low ATP utilization (6, 7). The biochemically-defined super-

relaxed (SRX) myosin state with low ATP turnover state has been associated with the structurally-defined IHM, where the two S1 myosin heads in complex with ADP, inorganic phosphate, and magnesium (the M.ADP.Pi state) are sequestered into the folded back state. (8, 9) (Figure 1A) This state is thought to be responsible for the slow rate of ATP turnover observed in stopped flow assays (10) and reduced ATP utilization (6) within the SRX state of muscle tissue (11). For these reasons, the IHM structure has received attention for its modulation of muscle contractility (12–15), roles in pathological states (5, 16–18), and as a therapeutic target (10, 19–21).

The IHM enables thick filaments to regulate sarcomere contractility and energy consumption by modulating myosin availability. Contractile magnitude is limited by the number of myosin heads available to interact with actin and consequently the force that can be generated by a thick filament. A rich set of structural and biochemical factors affect the structural stability of the IHM, including RLC phosphorylation, (22) myosin binding protein C phosphorylation, (23, 24) thick filament stress, (25) ionic strength, (20) and temperature (20, 26), and thick filament strain (25). Missense mutations in myosin can pathologically disrupt the natural equilibrium of free (i.e. recruitable) and sequestered myosin heads and lead to myopathies (3, 5, 16, 17). Myosin-targeted small molecules can similarly modulate IHM stability (10, 20). In previous work, our group has studied the effects of the naturally occurring small molecule, 2'-deoxy-ATP (dATP), on the structure, dynamics, and function of myosin. This ATP analogue affects overall actin-myosin crossbridge cycling, increasing the actin-activated ATPase activity of myosins by increasing the number of force-bearing cross-bridges and the rate of cross-bridge cycling (27). dATP increases the extent and rate of force development in skeletal (28) and cardiac (29, 30) muscle. In the stopped flow apparatus, dATP can completely eliminate the slow ATP turnover rate associated with the biochemically-defined SRX state of myosin and populate the disordered relaxed state (DRX) that has a ~10-fold faster ATPase activity (10). In demembranated and intact muscle, dATP repositions myosin heads farther away from the thick backbone and closer to thin filaments, as observed with small angle X-ray diffraction, and it increases the weak binding of myosin to thin filaments in resting muscle, as measured with sinusoidal stiffness analysis. (31, 32) These observations indicate that dATP amplifies muscle contraction through dual mechanisms of destabilizing the IHM state and by accelerating cross-bridge cycling. Such increases in power output with proportional changes in dATPase activity have led to efforts to increase dATP levels in cardiac muscle through gene therapy approaches to rescue depressed contraction associated with heart failure (33–38). Additionally, dATP may be used as a research tool to probe the molecular mechanisms by which the IHM is destabilized.

The structural dynamics that regulate IHM conformation and stability remain unclear. Gains in the resolution of structures obtained with cryogenic electron microscopy (cryo-EM) have paved the way for

3

studies of the IHM structure. (7, 8, 39–43) Grinzato *et al.* solved a high-resolution (3.6 Å) structure of IHM state human β-cardiac myosin. (44) Dutta *et al.* solved structures of mavacamten-stabilized human ventricular C-zone thick filaments that include IHM state β-cardiac myosin (6.4 Å resolution) from human cardiac ventricular tissue. (45) Tamborrini *et al.* solved structures of mavacamten-stabilized mouse C-zone thick filaments (18 Å resolution) as well as thin filaments using mouse cardiac ventricular myofibrils (46). These studies have examined IHM conformations in static environments and thick filament structures were obtained in the presence of mavacamten, which stabilizes an otherwise dynamic and heterogeneous multiprotein complex. Little is known about the structures and dynamics of myosin under conditions that destabilize the IHM. Here, we utilize microsecond scale molecular dynamics (MD) simulations to investigate the intrinsic dynamics of the IHM structure and its dynamics under a destabilizing condition in which dADP.Pi is bound to both the blocked and free head. Our study is comprised of two simulated IHM myosin systems: each system contains two copies of human β-cardiac myosin, essential light chain, and regulatory light chain along with solvating water molecules that amount to ~600k atoms. The first system is based on a model of the IHM constructed by rigidly docking myosin into a low resolution (28 Å) map of the cardiac thick filament (16, 41) and 11µs long simulations were performed using the Anton 2 supercomputer (47). The simulations represent the longest simulations of human β-myosin in the IHM state ever performed at atomic resolution and in explicit solvent and were made possible by unique access to the specially designed Anton 2 supercomputer. A high resolution (3.6 Å) cryo-EM structure of the IHM structure was solved by the Houdusse group (PDB: 8ACT) after simulations were performed on Anton 2.(44) Since several structural differences between the two structures obtained in different structural environments and at drastically different resolutions (28 vs 3.6 Å) have been noted, we also performed 200 ns long simulations using GPU accelerated computing for comparison (44). Both systems were simulated under two conditions in which either ADP.Pi (M.ADP.Pi) or dADP.Pi (M.dADP.Pi) was bound in the nucleotide binding pockets of both the blocked head and free head. The results of the Anton 2 simulations are presented in the main text and the remaining simulations are discussed in the supporting material. As observed in prior studies, (32, 48, 49) we found that the dADP nucleotides were more dynamic than their ADP counterparts and formed distinct interactions with myosin. Altered myosin:nucleotide contacts propagated throughout the complex and modulated of residue-residue interactions at the BH – FH interface and contemporaneously altered structures and dynamics of the tail and motor domain-S2 interactions. Our simulations model sites of dynamic behavior in the sequestered state and make predictions of the mechanisms by which dADP.Pi recruits heads from sequestered, inactive conformations.

Theoretical Methods

Two 11 microsecond-long molecular dynamics (MD) simulations of IHM state myosin (M.ADP.Pi) were performed with either ADP.Pi or dADP.Pi in the nucleotide binding pocket using *Anton 2* (47). In the 'reference' system (M.ADP.Pi), ADP, inorganic phosphate (P_i), and Mg^{2+} were bound in nucleotide binding pockets of both the blocked and free head. In the 'destabilizing conditions' system (M.dADP.Pi), both ADP molecules were replaced by dADP. These systems were prepared for production runs using the *AMBER20* MD package. One simulation of each system was performed for ~11 microseconds (μs) using the *Desmond MD* package. Detailed methods for system development, parameterization, simulation, and analysis may be found in the Supporting Material.

Results

The functionally inhibited IHM state undergoes conformational fluctuations. We evaluated large-scale conformational changes observed during MD using the C_α root-mean-square deviation (RMSD) of the simulations after alignment to the equilibrated structures. Following alignment to all C_α atoms, the M.dADP.Pi simulation experienced greater structural deviations from the equilibrated conformation, but the extent of structural deviation varied among the different structural regions. 13 different RMSD calculations were performed, each associated with unique subsets of protein C_α atoms (Table 1). For 10 out of these 13 calculations, the M.dADP.Pi simulation experienced greater deviations from the reference structure than the M.ADP.Pi simulations (Table 1). The LCBD, coiled-coil tails, and light chains had the greatest change in C_α RMSD relative to the equilibrated structures. Similar trends were observed for the 8ACT-based simulations (SI Table 1). Replacement of ADP.Pi by dADP.Pi also amplified structural changes in the free head motor domain.

The simulated IHM systems contain many flexible components: to assess structural diversity within the simulations, we re-aligned the trajectories to a set of 'minimally dynamic residues' identified via the *mdlovofit* algorithm. (50–52) This subset contains 1,482 C_α atoms in the motor domains and motor domain-binding regions of the tail. After alignment to the *mdlovofit* subset we calculated the C_α RMSD (Figure 2A) and RMSF (Figure 2B) for all C_α atoms as well as the difference in RMSF between the M.ADP.Pi and M.dADP.Pi simulations (Figure 2C). The M.dADP.Pi system remained more dynamic and sampled conformations further away from the equilibrated reference structure than the M.ADP.Pi system (Figure 2A-C). In both simulations, residues in the FH had higher atomic fluctuations than in the BH, and residues in the light chain-binding portions of the tail, the ELC, and RLC had the greatest overall atomic fluctuations (Figure 2B-C). The RMSF values were mapped onto the equilibrated structures for the M.ADP.Pi and M.dADP.Pi simulations (Figure S1) We subsampled the trajectories at 6 ns intervals and calculated the pairwise C_α RMSD between simulation snapshots (Figure 2D,F) and clustered the MD trajectories using the k-means algorithm (Figure 2E,G). The pairwise C_α RMSD values show that the M.dADP.Pi system had

greater conformational changes over the course of the trajectory, with a major shift occurring around ~2 μs. We clustered the trajectories after alignment to the *mdlovofit*-selected C_α atoms using the 'cluster' command in *cpptraj* using the k-means algorithm and the optimal k-value for clustering based on the elbow point in the SSR/SST curves, which reports on the conformational variance explained by the clustering. The k-means cluster representatives show that structural changes in the light chain binding regions of the tail and the BH – FH interface contributed most to the structural differences between the ADP.Pi and dADP.Pi simulations (Figure 2E,G). This coarse-grain analysis of the IHM dynamics demonstrates that in solution the IHM is a dynamic protein complex that samples multiple conformations and that increased structural changes due to the replacement of ADP.Pi by dADP.Pi are observable on microsecond timescales. The greatest changes relative to the starting model occurred during the equilibration phases and within the first ~2 μs of the production phases. This can be described by a change in the angles formed by the light chain binding domain (LCBD) of the tail, a reorganization of the head-head interface, and a rotation of the free head around the S2 tail (Figure 2H). These changes persisted for the duration of the simulations (Figure 2I).

Table 1. C_α RMSD of select myosin regions highlights that the dADP.Pi simulations experienced greater average structural deviations from the equilibrated starting conformation.

	Region	Myosin + ADP.Pi		Myosin + dADP.Pi		Δ Average[8] (dADP.Pi - ADP.Pi)
		Avg. (Å)	St. Dev. (Å)	Avg. (Å)	St. Dev. (Å)	
IHM	**All[1]**	8.1	0.7	9.3	1	1.2
Blocked Head	**All[2]**	4.4	0.3	6	0.8	1.6
	Motor Domain[3]	3.2	0.2	3.3	0.3	0.1
	Converter[4]	3.6	0.2	3.9	0.6	0.3
	Tail[5]	5	0.7	9.4	1.6	4.4
	ELC[6]	3.4	0.4	8	0.4	4.6
	RLC[7]	7.5	0.6	8.7	0.7	1.2
Free Head	**All[2]**	5.8	0.4	5.7	0.7	-0.1
	Motor Domain[3]	2.7	0.3	4.5	0.7	1.8
	Converter[4]	1.5	0.1	1.5	0.2	0
	Tail[5]	5.5	0.7	5.8	1.3	0.3
	ELC[6]	4.9	0.6	4.5	1.1	-0.4
	RLC[7]	4.8	0.4	8.5	1.5	3.7

1. All Cα atoms from all residues were used in both the alignment and calculation

2. All Cα atoms in the of the blocked head (BH + ELC + RLC) or free head (FH + ELC + RLC) were used in the alignment and calculation
3. Myosin motor domain Cα atoms (residues 1-706) of the BH or FH were used in the alignment and calculation
4. Myosin tail Cα atoms (residues 769-938) of the BH or FH only were used in the alignment and calculation
5. Myosin converter domain Cα atoms (residues 706-768) of the BH or FH were used in the alignment and calculation
6. All Cα atoms in the ELC of the BH or FH were used in the alignment and calculation
7. All Cα atoms in the RLC of the BH or FH were used in the alignment and calculation
8. Positive values indicate greater structural deviations were observed in the M.dADP.Pi simulation; negative values indicate greater structural deviations were observed in the M.ADP.Pi simulation
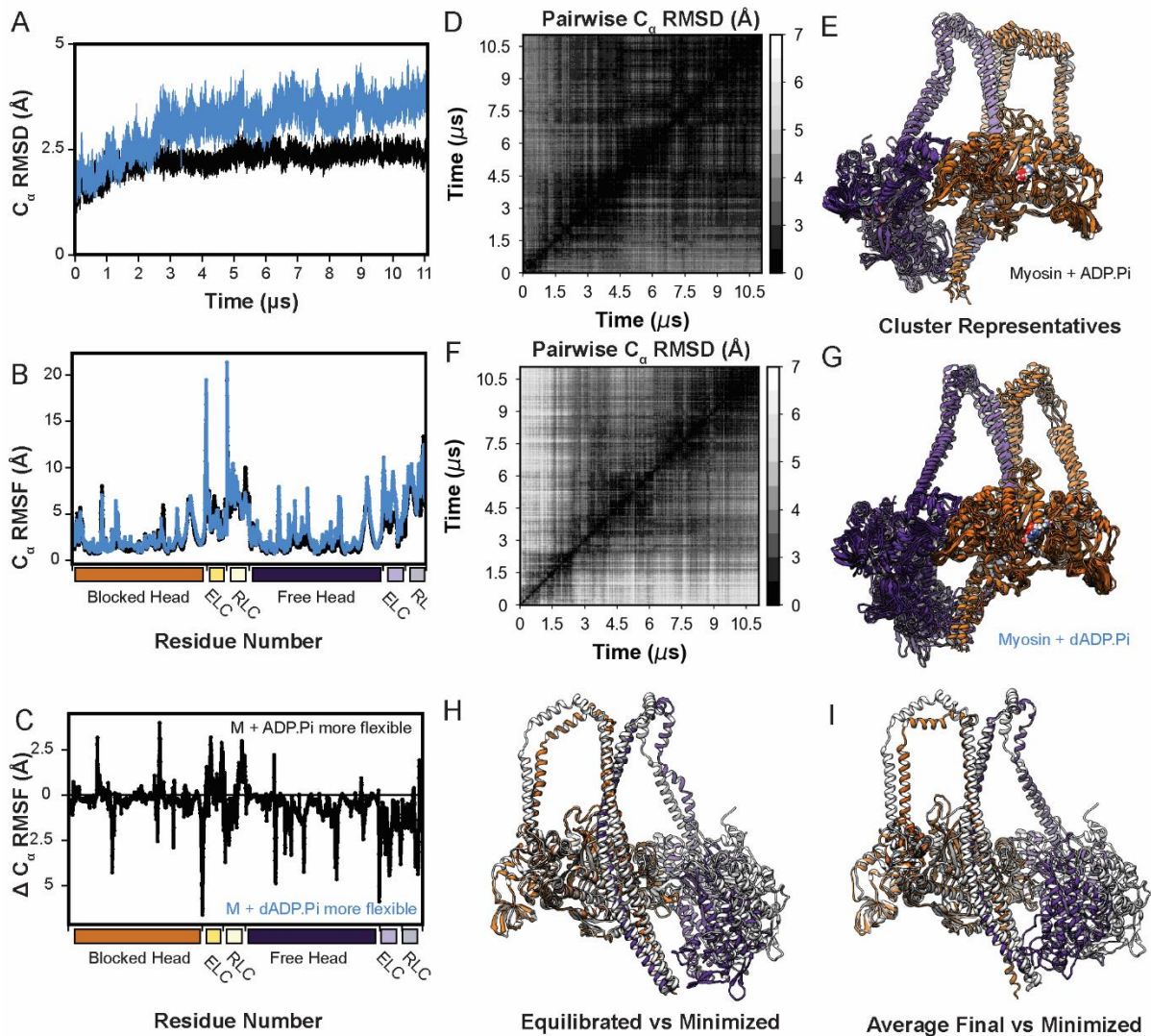

Figure 2. Overall dynamics of IHM myosin. (A) C_α RMSD of the IHM M.ADP.Pi (black) and IHM M. dADP.Pi (blue) simulations as a function of simulation time. RMSDs were calculated after alignment to stable residues identified by *mdlovofit*. (B) C_α RMSF of the IHM M.ADP.Pi (black) and M.dADP.Pi (blue) simulations as a function of residue number. (C) The difference in C_α RMSF between the M.ADP.Pi and dADP.Pi-bound myosin simulations. Positive values indicate that residues were more flexible in the M.ADP.Pi simulation. Matrices in (D) and (F) plot the pairwise C_α RMSD between simulation snapshots for the M.ADP.Pi and M.dADP.Pi simulations; lighter values indicate higher RMSDs and greater structural

changes over time. The structures in (E) and (F) correspond to the k-means cluster representatives for the M.ADP.Pi and M.dADP.Pi simulations, respectively. The ELC and RLC ribbons are not shown here. A comparison of the MD-equilibrated structure versus the minimized model (H) highlights the conformational changes in the LCBD and free head orientation that persisted (I) throughout the simulations.

Conformational diversity of the blocked and free heads. Next, we performed a conformational analysis that considered the blocked and free heads in isolation: we repeated the C_α RMSF and clustering analyses after alignment of the trajectories to residues in either the blocked head or free head. The blocked head had the least conformational variability, likely due to the interactions with other protein components that restrict its conformational heterogeneity (Figure S2A,B, Figure S3A,C). Within the upper 50 kDa region of the motor domain the 'O helix' (residues 417-447) acts as a central structural support for helix G (residues 219-232), a helical bundle (residues 268-322), loop 2 (Residues 623-644), the cardiomyopathy loop (residues 401-417) and loop 4 (residues 361-378). In our simulations we found that the O-helix and these flanking regions were the most dynamic sites in both the blocked head and free head (Figure S2). The free head tended to have a more flexible upper 50 kDa domain than the blocked head and flexibility of both the blocked and free head upper 50 kDa domains was amplified in the M.dADP.Pi simulations (Figure S3). The free head conformation was less restricted, but in all simulations, it tended to twist so that loop 2, loop 4, and/or the cardiomyopathy loop of the free head could interact with the C-terminus of S2 (Figure S4).

dADP.Pi formed distinct interactions with myosin motor domains To identify the molecular origins of the dynamic differences between M.ADP.Pi and M.dADP.Pi, we compared the BH nucleotide binding pockets when bound to the two different nucleotides. Nucleotide dynamics were evaluated by monitoring 6 dihedral angles that describe (d)ADP structure using internal coordinates, as previously described (48). The 6 calculated dihedral angles were defined as: θ_1 (atoms: O1B-PB-O3A-PA), θ_2 (PB-O3A-PA-O5′), θ_3 (O3A-PA-O5′-C5′), θ_4 (PA-O5′-C5′-C4′), θ_5 (O5′-C5′-C4′-O4′), and θ_6 (O4′-C1′-N9-C8) (Figure 3A). Ramachandran-style dihedral angle maps (θ_1 vs θ_2, θ_3 vs θ_4, and θ_5 vs θ_6) describe the relative orientation of the phosphate groups, the sugar ring, and the purine ring. Nucleotide conformation was strongly related to the interactions formed with residues in the nucleotide binding pocket of myosin (Figure 3B). The dihedral maps show that ADP.Pi and dADP.Pi were dynamically and structurally distinct and that the dADP nucleotides in both the blocked and FHs sampled a greater degree of conformational space and had greater conformational entropy (Figure 3C). These results mirror prior studies of dATP/dADP demonstrating that dADP (Figure 3E) is an intrinsically more dynamic nucleotide than ADP (Figure 3F) when bound to myosin (48, 49).
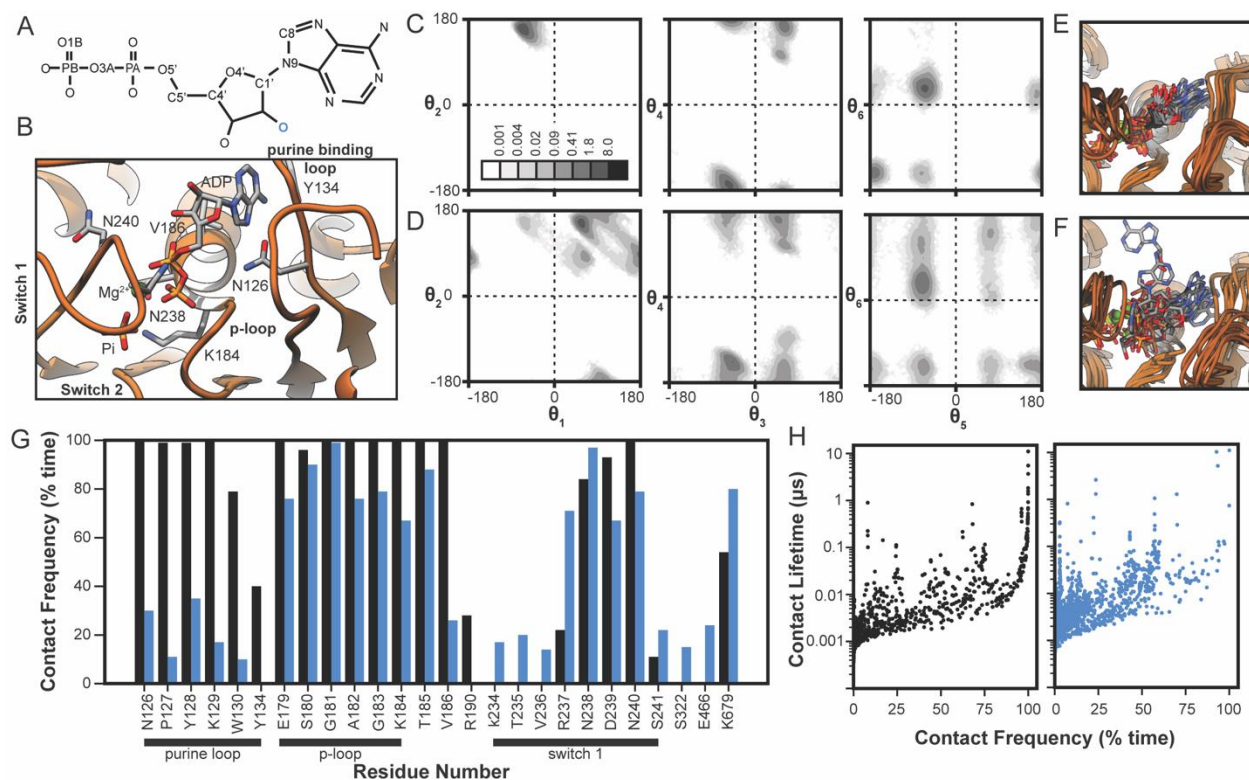
Figure 3. dADP was more dynamic than ADP. (A) The structure of ADP is shown. The names of atoms that define the dihedral angles are provided in the structure and the 2' oxygen atom that is absent in dADP is colored blue. (B) A structure of the equilibrated nucleotide binding pocket of the blocked head identifies functional residues in the purine binding loop, phosphate binding loop, and switch 1 that participate in interactions with ADP. Maps of 6 dihedral angles collectively describe the nucleotide conformations of ADP (C) and dADP (D) within the nucleotide pocket of the blocked head. (θ_1, θ_2) describes the relative orientation of the terminal phosphate groups (left); (θ_3, θ_4) describes the orientation of the sugar relative to the alpha phosphate (center); (θ_5, θ_6) describes the orientation of the purine ring relative to the sugar ring (right). Dihedral angle data were allocated to 5° x 5° bins and shaded according to the number of conformers allocated to each bin. Inset color scale indicates the percentage of the simulated ensemble allocated to each 5° x 5 ° bin. Evenly spaced snapshots of ADP.Pi (E) and dADP.Pi (F) demonstrate the differences in the nucleotide dynamics. (G) The percent of simulation time for which different myosin residues (x -axis) interacted with ADP (black) and dADP (blue) are shown. Calculations were performed at the residue level: a nucleotide-residue pair was considered in contact if at least one pair of heavy atoms had a distance < 5 Å. Nucleotide-myosin interactions were nucleotide-dependent. (H) Atom-atom contact lifetimes as a function of contact frequency are shown for M.ADP.Pi (black, left) and M.dADP.Pi (blue, right) interactions within the blocked head. Calculations were performed at the atom level: each point corresponds to a contact between a unique pair of heavy atoms.

The distinct dynamics of ADP and dADP in the BH resulted in distinct interactions between the nucleotides and myosin residues within the nucleotide binding pocket. We measured the percent simulation time for which the nucleotides interacted with a myosin residue (Figure 3G). In the M.ADP.Pi simulation, the nucleotide retained its starting conformation that has been observed in structure of pre-powerstroke (1. M.ADP.Pi) state myosin. The purine ring of the nucleotide interacted with the purine binding loop (residues

9

126-134), the phosphate groups remained surrounded by the phosphate binding loop (residues 178-184), and the sugar ring (including 2'/3' hydroxyl groups) formed transient interactions with residues in switch 1 (residues 232-244). In contrast, the more dynamic dADP formed fewer interactions with purine loop residues, fewer interactions with phosphate binding loop residues, and altered interactions with switch 1(Figure 3G). Finally, we examined the average duration of a nucleotide:myosin contacts at the atomic level (Figure 3H). We found that dADP participated in fewer long-lived (i.e. > 75% contact frequency) interactions and that the average atom-atom contact lifetime was decreased for M.dADP.Pi (Figure 3H). Similar behavior was observed for the nucleotides in the FH and in the 8ACT simulations (Figure S5).

Altered nucleotide-myosin interactions propagated throughout the IHM structure. To determine the impact of the more dynamic dADP.Pi on IHM dynamics, we next analyzed residue-residue contacts across the IHM structure. For each MD snapshot, two residues were considered in contact if at least one pair of heavy atoms between them were within 5Å of one another. We compared the residue-residue contacts formed in the simulations and only considered contacts which were present for at least 10% of time in either simulation. Contacts were considered as altered by dADP.Pi if there was at least a 30% difference in the percentage of simulation time that the contact was present in the two simulations. With this conservative definition, of the ~29,000 observed residue interactions, ~3,500 contact pairs differed by at least 30% between the M.ADP.Pi and M.dADP.Pi simulations. We mapped the altered interactions onto the equilibrated starting structure of the M.ADP.Pi simulation (Figure 4A). The altered contacts clustered in three regions of the IHM: the upper 50 kDa domains of both the BH and FH, the BH – FH interface, and the interfaces between the myosin heavy chains and light chains (Figure 4A). The pattern of contacts altered by dADP.Pi suggest that changes in the nucleotide binding pocket allosterically propagated through the upper 50 kDa domain of the BH and result in altered interactions made by nearby loops (residues 275-282, 311-324), the O-helix (residues 416-448), and ultimately the functional loops: loop 2 (residues 622-645), loop 4 (residues 361-377), and the cardiomyopathy loop (residues 402-416) (Figure 4A). This allosteric effect of dADP.Pi has been observed in prior MD simulations and the pathway though which dADP/dATP operates appears conserved; however, the effect propagated more slowly in the IHM simulations, possibly due to greater conformational constraints imposed by the IHM structure. However, prior simulations have used different MD force fields and have simulated different chemomechanical states, precluding a definite comparison of the 'strength' of dATP's effect on myosin structure.
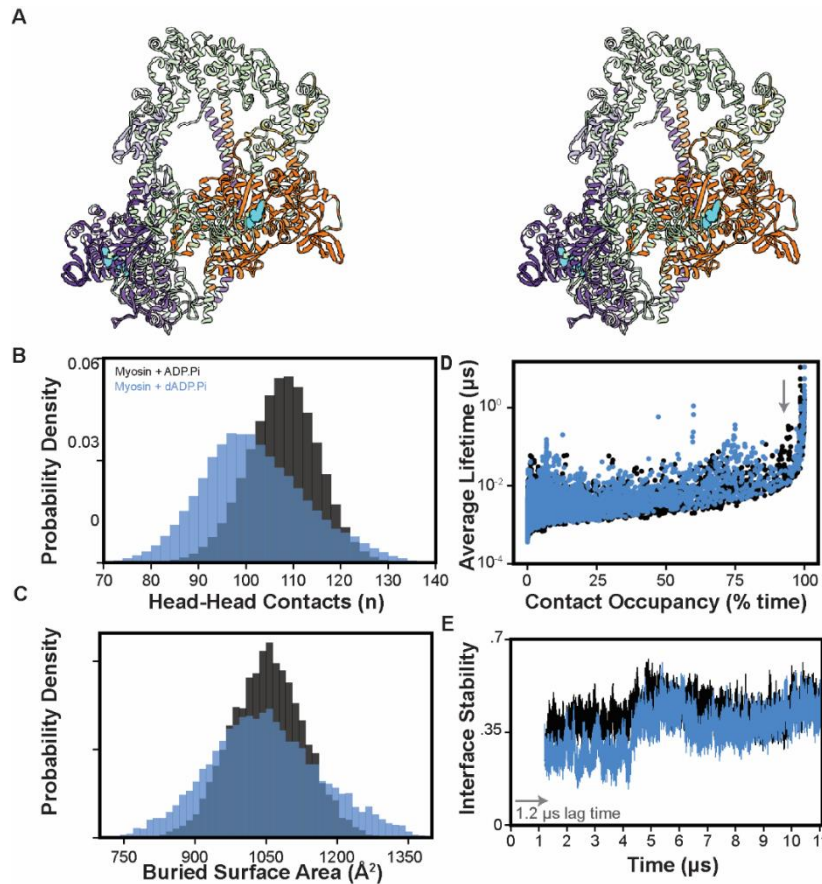
Figure 4. Altered nucleotide dynamics led to altered conformations of the motor domain. (A) Stereo image of the IHM depicting structural changes between the ADP.Pi and dADP.Pi simulations. Residues that had altered contacts are shown in lime green. (B) The total number of interacting residue pairs between the blocked head and free head were monitored over the course of the simulation. (C) The buried surface area of the interface between the blocked head and free head was variable during the simulations and was more variable in the M.dADP.Pi simulation. (D) Contact lifetimes versus contact occupancies for the atom-atom interactions between the blocked head and free head in the ADP.Pi (black) and dADP.Pi (blue) simulations. (E) Jaccard index calculated for the set of atoms participating in the blocked head – free head interface as a function of time with a 1.2 microsecond lag.

Conformational heterogeneity at the blocked head – free head interface In the IHM state, the two motor domains form an evolutionarily conserved interface in which the mesa (3, 42) of the BH docks against the the coiled-coil S2 tail and the actin binding regions of the BH upper 50 kDa domain dock against the converter domain of the FH. Changes in the internal structure of the upper 50 kDa domain (Figure 4A) of the BH led to modulation of the BH – FH interface. To assess the stability of the BH – FH interface, we tracked the interacting residue-residue pairs between the BH and FH over time. Independent of the bound nucleotide, we found that the interface was intrinsically dynamic. The number and composition of interacting residue pairs was variable in the M.ADP.Pi simulation. The BH – FH interaction was not a fixed interface, but like other protein complexes the interface was fluid and dynamic. (53) In a time average, M.dADP.Pi had 7% fewer BH – FH interactions than M.ADP.Pi, though there were conformations observed with increased and decreased BH – FH interactions (Figure 4B). The surface area of the buried BH – FH interface (Figure 4C) was similar in both simulations, though there was more heterogeneity in M.dADP.Pi.

For either case, the conformations explored by M.dADP.Pi were more heterogeneous. The average contact lifetimes for atom-atom pairs in the two simulations (Figure 4D) and observed that the M.dADP.Pi simulation had slightly fewer long-lived inter-head contacts than the M.ADP.Pi simulation. (Figure 4D) To evaluate the endurance of contacts at the BH – FH interface, we calculated the Jaccard Index (JI) of residue pairs in the BH – FH interface for every frame i versus frame i-10,000 (a 1.2 microsecond lag, Figure 4E). Here, the JI measures the fraction of residue pairs that remain in contact after a lag time; a value of 0 indicates all interacting residue pairs have changed and a value of 1 indicates all interacting residue pairs have remained. There were low values of the Jaccard index for both simulations during the first ~4 microseconds of the trajectories, though the value for M.dADP.Pi was lower, indicating a greater rate of change. By the end of the simulations, the interfaces for both models stabilized to a similar degree, but still retained some heterogeneity, as has been reported in studies of other protein interfaces (53). Changes in the structure of the upper 50 kDa domain associated with the replacement of ADP.Pi by dADP.Pi ultimately led to a distinct interface formed between the BH and FH. Loop 4 and the cardiomyopathy loop of the blocked head were the least stable regions of the head-head interface in the M.dADP.Pi simulations. At the start of both simulations, the cardiomyopathy loop of the blocked head interacts with the mesa of the free head and was stabilized by two salt bridges (BH R403 to FH E170 and BH E409 to FH R249). Over the course of the M.dADP.Pi simulation these interactions were lost and the BH cardiomyopathy loop detached from the free head and instead interacted with loop 2 of the blocked head. In structures of the IHM loop 4 of the blocked head weakly interacts with the converter domain and relay helix of the free head. In all MD simulations we found that loop 4 became more buried from solvent and formed more interactions with the converter domain and relay helix of the free head. Finally, we assessed the strength of nonbonded (i.e. van der Waals and electrostatics) interactions between the two heads at the BH – FH interface using the *energy* command of *cpptraj*. On average, the M.ADP.Pi interaction energy was -978 ± 83 kcal/mol (errors are standard deviation) and the M.dADP.Pi interaction energy was -837 ± 98 kcal/mol, a 14% decrease.

Conformational heterogeneity within the light chain binding domain. The second site of major conformational change identified by our contact analysis were the regions of myosin that interacted with the light chains. In addition, there are several residues in the pliant region of the tail that form hinge sites that enable the heads to adopt various orientations and likely contribute to the formation of the IHM. To analyze the tail conformations in our simulations, we measured four interhelical angles formed between the flexible joints of the motor domain, lever arm, and S2 tail (Figure 5A). Angle 1 was defined by residues 699-706 and 770-783; angle 2 by 786-800 and 812-822, angle 3 by 812-822 and 831-838, and angle 4 by 831-383 and 845-872. After the equilibration phase that occurred at the beginning of the simulations, the hinge sites sampled conformations around an average value. For most angles the average values were

different in the M.ADP.Pi and M.dADP.Pi simulations (Figure 5B). There were also differences in the average angles sampled by the BH and FH heavy chains (Figure 5B). The distinct bending of the tails in the simulations was associated with a change in the orientation of the FH relative to the S2 tail and the BH (Figure S4). In these simulations, the conformation and dynamics of the pliant region of the tail were nucleotide-sensitive and related to changes in the BH – FH interface. Thus, our model predicts that the tail conformation can adjust to accommodate alternate BH – FH orientations (or vice-versa).
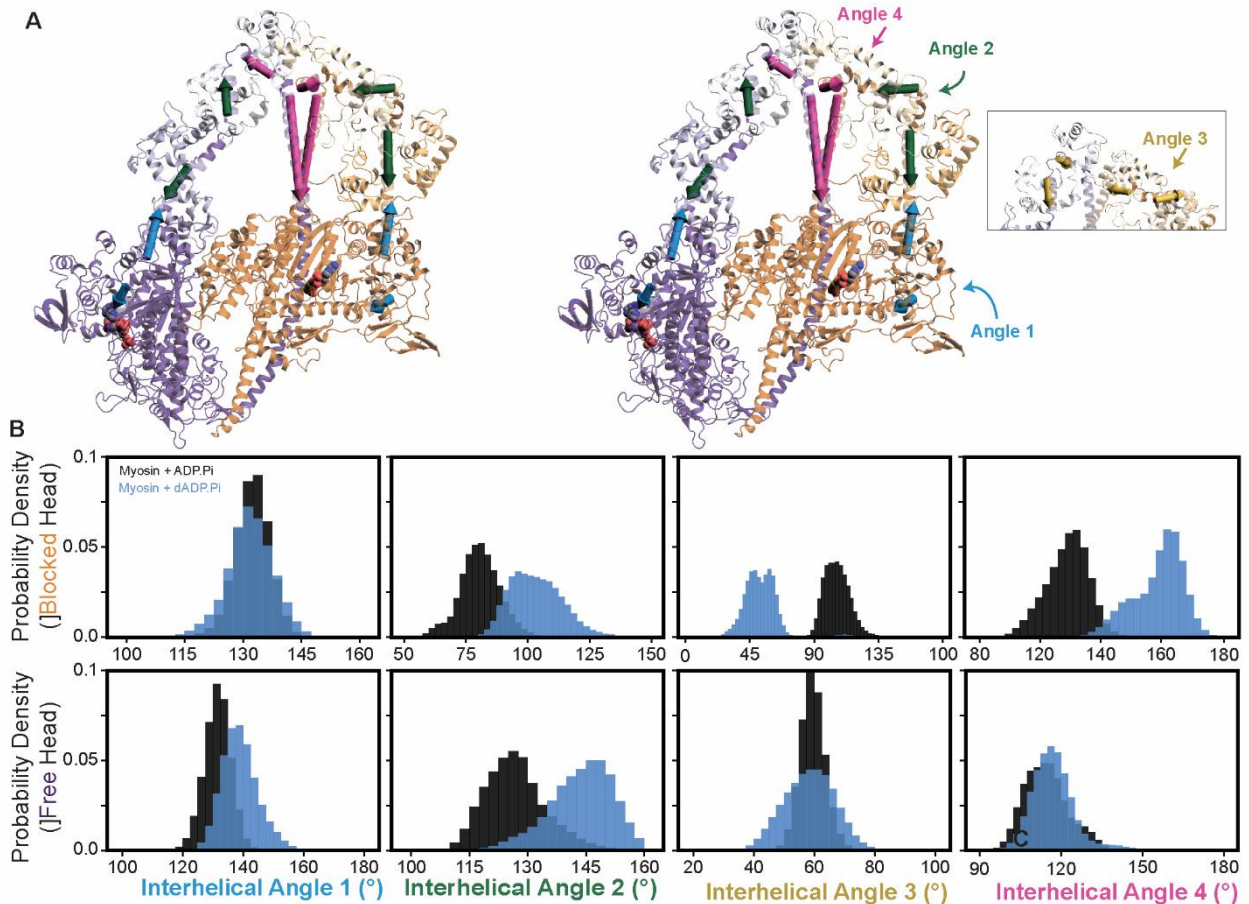

Figure 5. The tail of the free head adopted a distinct, 'crimped' conformation in the M.dADP.Pi simulations. Four interhelical angles (angles 1-4, blue, green, yellow, and magenta respectively) were analyzed over the course of the simulations. Panel (A) depicts a stereo image of the IHM with the four interhelical angles superimposed on the structure. (B) Distributions of the four interhelical angles calculated over the simulations are shown for the angles within the blocked head (top row) and free head (bottom row) for both the M.ADP.Pi (black) and M.dADP.Pi (blue) simulations.

Discussion

The conformation and dynamics of the pliant region are correlated with the BH – FH interface. Our simulations provide insights into the structural mechanisms by which the conformation and dynamics of the tail/light chain modify IHM stability. First, our M.dADP.Pi simulation predicts that structural changes at the BH – FH interface occurred alongside changes in the conformations of S2 and the pliant region of the tail. It has been previously shown that phosphorylation of the regulatory light chain (22) modifies the stability of the IHM and, further, that mutations in the pliant region of the tail can (de)stabilize the IHM. (5) Thus, we propose that flexibility in the tail of the BH is necessary for the heads to form distinct relative orientations and to ultimately detach from one another. The hinge sites C-terminal to the RLC binding site (angles 2 and 3, Figure 5) experienced the greatest changes in the two simulations and had high correlated motions, suggesting flexibility in this region is critical for native-like IHM stability. The large-scale structural changes corresponding to reorganization of the head interface and being of the tails occurred over 2-4 microseconds. This implies that the equilibration period for these IHM constructs is on the ~2 microsecond time scale, highlighting a need for long timescale simulations on specialized architecture or the development of accurate coarse-grained models for future investigations of the structural and dynamic behavior of the IHM. There are many HCM/DCM-associated mutations reported in the hinge regions of the tail, including R783H, R787C, A797T, L811P, F834L, and E846Q. Since these hinges had appreciable fluctuations even in the IHM state, our study warrants additional characterization of the effects of mutations in tail hinge sites on IHM stability and thick filament organization.

The importance of the pliant region and dependence of IHM conformation and dynamics on environment. Analysis of the M.ADP.Pi simulation yields powerful insights into the intrinsic dynamics of myosin in the IHM state. As with any molecular dynamics study, the simulations presented here suffer from the *accuracy* and *sampling problems* (54), and the results must be interpreted through these limitations. First, these simulations were initiated from homology models constructed using low-resolution (> 10 Å) cryoEM maps and did not begin from empirically observed structures (the *accuracy* problem). Grinzato *et al.* showed that initial homology models differed from empirical models with respect to the angles adopted by the tail and the residues participating in the BH – FH interface (44). A notable difference is in the conformation of the BH pliant region. In the pre-production portion of our study, we observed that the hinges in this region of the homology model transitioned to conformations similar to those in the empirical cryoEM model, though an exact correspondence was not observed. (Movie S1) Second, these simulations have each probed 11 microseconds of IHM dynamics, which is extensive given contemporary MD capabilities but limited in biochemical contexts (the *sampling* problem). Given current structural data and simulations, it is not possible to assess the extent of sampling obtained in these simulations nor is it possible to assess whether the simulations have adopted a local conformational minimum or are *en route* to it (55).

dADP.Pi modified the IHM conformation by modifying upper 50 kDa domain structure and the BH – FH interface Despite dATP/dADP differing from ATP/ADP structurally by only a single atom, the two nucleotides have distinct effects on the stability of the inactive conformation of myosin, as well as on the kinetics of actively cycling myosin heads (10, 31, 32). Previously, we have observed nucleotide-dependent dynamics for multiple myosin sequences and in multiple chemomechanical states using diverse MD force fields and simulation engines. (31, 48, 49, 56) We have consistently observed that the two nucleotides sample distinct conformational ensembles, form distinct sets of interactions with the nucleotide binding pocket (particularly switch 1 and the purine binding loop), and each impact the organization of residues in the upper 50 kDa domain of myosin. Here, we used dADP as a tool to understand the factors that destabilize the IHM. We observed that replacement of ADP.Pi by dADP.Pi modified myosin structure via structural changes that propagated along an allosteric pathway passing through switch 1 and the upper 50 kDa domain. Structural changes at the BH – FH interface resulted in a 14% decrease in interaction energy in the presence of dADP. The high degree of heterogeneity observed among the interacting residue pairs and buried surface area at the BH – FH interface was reflected in the variance of the interaction energy. Our results suggest the allosteric changes to myosin caused by dADP can weaken the critical BH – FH interface. The observed allosteric effect suggests that amino acid mutations within the upper 50 kDa domain have the potential to modify the upper 50 kDa domain structure, the presentation of charges and patterns of charged residues on the motor domain surface, and ultimately the stability of the IHM even if they do not directly participate in BH – FH interactions. Our simulations predict that changes in interactions made by residues like N232, D239, R243, Y283, S291, D309, A381, L427, and V606 can influence the conformation of the portion of the blocked head that interacts with the free head. In a recent review by Spudich and coworkers it is shown that HCM-associated myosin mutations tend to increase in the number of ON state myosins independent of the location of the mutation in the protein, motivating further study of the allosteric connections in this complex motor that can regulate the stability of various structural states. (57) Disease associated mutations in this region merit further study to uncover any allosteric changes that can transmit to the blocked head – free head interface.

We speculate that the tail conformation observed in recent cryoEM conformations is a rigid conformer that may be stabilized by mavacamten, which is reported to bind to the same binding pocket as omecamtiv mecarbil and affects the lever arm position (58). Modeling the pliant region and particularly the interface between the RLCs is challenging and is a point of structural heterogeneity among cryoEM models of the IHM. The higher resolution of residues within the BH – FH and BH – S2 interfaces coupled with the biomedical impact of disease associated mutations in the mesa have focused efforts on these regions (59–61). Many models of the pliant region and RLC have used molluscan RLC conformers as templates, and the correspondence of molluscan and mammalian light chain structures is unclear as molluscan RLCs can

bind Ca^{2+} to regulate thick filament activity (6[3]). Pliant region conformers have also been modeled using thick filament maps in which IHM motor domains form intermolecular interactions with neighboring IHMs, which may be heterogeneous (45, 46). Uncertainty around the pliant region and RLC conformation continues to impact structural and dynamical studies of the IHM. The Grinzato *et al.* model also indicated higher flexibility (lower resolution) within S2, the RLCs, and the light chain binding region of the tail. Flexibility within the pliant region may allow myosins to form the IHM in different thick filament geometries or to adopt distinct IHM conformers in different regions of the thick filament (63, 64). Flexibility among the hinge regions and heterogeneous interacts with other thick filament proteins may ultimately affect the rates of entry into and exit from the IHM. The simulations reported here indicate that these interhelical angles are flexible hinges and suggest a relationship between the conformations of the pliant regions and the BH – FH interface. However, the extent to which these simulations are 'correct' is unclear as the challenges associated with model building necessarily bias MD calculations. These findings should motivate increased attention to both the structure and dynamics of the pliant region and the RLC interface. Higher resolution structural insights into this region are needed as the structural factors impacting IHM stability extend beyond the myosin mesa. In future studies, MD simulations may explore accessible conformations of the pliant tail in different structural, physical, and chemical environments.

Comparison of dynamics of the different models. The high and low resolution cryoEM models of the human cardiac differed in two regions: the conformations adopted by the light chain binding region of the tail as well as the positioning of loop 4 of the blocked head. In our simulations we found that the light chain binding region was highly dynamic for both models. Maps of the MD-derived RMSF values superimposed onto the structure (Figure S1) match well to the resolution map in the 8ACT cryoEM study. From this observation and recent studies on HCM/DCM mutations we conclude that the light chain binding region is highly dynamic and a source of (de)stabilization for the IHM. Also common to all simulations performed here was that the free head tended to have greater conformational mobility than did the blocked head. Our simulations suggest that loop 4 of the blocked head forms a strong interface with the converter domain and relay helix of the free head than observed in structural studies. Based on these simulations and the observation that binding of dADP.Pi to the blocked head causes a conformational change that reduces interactions between the heads our simulations suggest that departure from the IHM begins when the blocked head – free head interface is sufficiently weakened to allow the free head to detach. This conformation barrier would be followed by extension of S2 at the hinge sites and detachment of the blocked head from S2, allowing the heads to join the pool of recruitable myosin motors.

Conclusions

We propose that our dADP.Pi simulations have captured structural changes that precede BH – FH dissociation and departure from the IHM conformation. Changes to the IHM under the simulated conditions involved a three-part mechanism. First, replacement of ADP by dADP led to a series of structural changes that propagated through the upper 50 kDa domain. Next, changes in the upper 50 kDa domain altered the BH – FH interface. Finally, changes in the BH – FH interface were met with structural changes in the pliant and LCBD regions. This indicates that structural perturbations distant from the mesa and BH-FH interface may pathologically or therapeutically modify IHM stability. Despite limitations, our study identifies new avenues for research into the structural and functional role of the IHM. In the context of the highly structured and dynamically-driven sarcomere, understanding protein structural ensembles is essential to model and engineer muscle behavior. The dynamic computational models utilized here indicate that the IHM is not a fixed, rigid state. Instead, the BH – FH interface and bent tails harbor intrinsic flexibility. These observations should inform ongoing and future experimental studies of HCM/DCM mutations and therapeutics that target the IHM.

Author Contributions

Designed research: M.C.C. and M.R.; Performed Research: M.C.C.; Analyzed Data: M.C.C.; Manuscript Writing: M.C.C., M.A.G., and M.R.

Acknowledgements

References

1. Sweeney, H.L., and D.W. Hammers. 2018. Muscle Contraction. *Csh Perspect Biol*. 10:a023200.

2. Sweeney, H.L., and A. Houdusse. 2010. Structural and Functional Insights into the Myosin Motor Mechanism. *Annu Rev Biophys*. 39:539–557.

3. Spudich, J.A. 2015. The myosin mesa and a possible unifying hypothesis for the molecular basis of human hypertrophic cardiomyopathy. *Biochem Soc T*. 43:64–72.

4. Brown, J.H., V.S.S. Kumar, E. O'Neall-Hennessey, L. Reshetnikova, H. Robinson, M. Nguyen-McCarty, A.G. Szent-Györgyi, and C. Cohen. 2011. Visualizing key hinges and a potential major source of compliance in the lever arm of myosin. *Proc National Acad Sci*. 108:114–119.

5. Morck, M.M., D. Bhowmik, D. Pathak, A. Dawood, J. Spudich, and K.M. Ruppel. 2022. Hypertrophic cardiomyopathy mutations in the pliant and light chain-binding regions of the lever arm of human β-cardiac myosin have divergent effects on myosin function. *Elife*. 11:e76805.

6. Ferenczi, M.A., E. Homsher, R.M. Simmons, and D.R. Trentham. 1978. Reaction mechanism of the magnesium ion-dependent adenosine triphosphatase of frog muscle myosin and subfragment 1. *Biochem J*. 171:165–175.

7. Wendt, T., D. Taylor, K.M. Trybus, and K. Taylor. 2001. Three-dimensional image reconstruction of dephosphorylated smooth muscle heavy meromyosin reveals asymmetry in the interaction between myosin heads and placement of subfragment 2. *Proc. Natl. Acad. Sci.* 98:4361–4366.

8. Woodhead, J.L., F.-Q. Zhao, R. Craig, E.H. Egelman, L. Alamo, and R. Padrón. 2005. Atomic model of a myosin filament in the relaxed state. *Nature*. 436:1195–1199.

9. Chu, S., J.M. Muretta, and D.D. Thomas. 2021. Direct detection of the myosin super-relaxed state and interacting-heads motif in solution. *J. Biol. Chem.* 297:101157.

10. Walklate, J., K. Kao, M. Regnier, and M.A. Geeves. 2022. Exploring the super-relaxed state of myosin in myofibrils from fast-twitch, slow-twitch, and cardiac muscle. *J Biological Chem*. 298:101640.

11. Stewart, M.A., K. Franks-Skiba, S. Chen, and R. Cooke. 2010. Myosin ATP turnover rate is a mechanism involved in thermogenesis in resting skeletal muscle fibers. *Proc National Acad Sci*. 107:430–435.

12. Jung, H.S., S. Komatsu, M. Ikebe, and R. Craig. 2008. Head–Head and Head–Tail Interaction: A General Mechanism for Switching Off Myosin II Activity in Cells. *Mol. Biol. Cell*. 19:3234–3242.

13. Irving, M. 2017. Regulation of Contraction by the Thick Filaments in Skeletal Muscle. *Biophys. J.* 113:2579–2594.

14. Lewis, C.T.A., and J. Ochala. 2023. Myosin Heavy Chain as a Novel Key Modulator of Striated Muscle Resting State. *Physiology*. 38:3–9.

15. Brunello, E., L. Fusi, A. Ghisleni, S.-J. Park-Holohan, J.G. Ovejero, T. Narayanan, and M. Irving. 2020. Myosin filament-based regulation of the dynamics of contraction in heart muscle. *Proc. Natl. Acad. Sci.* 117:8177–8186.

16. Alamo, L., J.S. Ware, A. Pinto, R.E. Gillilan, J.G. Seidman, C.E. Seidman, and R. Padrón. 2017. Effects of myosin variants on interacting-heads motif explain distinct hypertrophic and dilated cardiomyopathy phenotypes. *Elife*. 6:e24634.

17. Sarkar, S.S., D.V. Trivedi, M.M. Morck, A.S. Adhikari, S.N. Pasha, K.M. Ruppel, and J.A. Spudich. 2020. The hypertrophic cardiomyopathy mutations R403Q and R663H increase the number of myosin heads available to interact with actin. *Sci Adv*. 6:eaax0069.

18. Nag, S., D.V. Trivedi, S.S. Sarkar, A.S. Adhikari, M.S. Sunitha, S. Sutton, K.M. Ruppel, and J.A. Spudich. 2017. The myosin mesa and the basis of hypercontractility caused by hypertrophic cardiomyopathy mutations. *Nat. Struct. Mol. Biol.* 24:525–533.

19. Anderson, R.L., D.V. Trivedi, S.S. Sarkar, M. Henze, W. Ma, H. Gong, C.S. Rogers, J.M. Gorham, F.L. Wong, M.M. Morck, J.G. Seidman, K.M. Ruppel, T.C. Irving, R. Cooke, E.M. Green, and J.A. Spudich. 2018. Deciphering the super relaxed state of human β-cardiac myosin and the mode of action of mavacamten from myosin molecules to muscle fibers. *Proc National Acad Sci*. 115:201809540.

20. Rohde, J.A., O. Roopnarine, D.D. Thomas, and J.M. Muretta. 2018. Mavacamten stabilizes an autoinhibited state of two-headed cardiac myosin. *Proc. Natl. Acad. Sci.* 115:E7486–E7494.

21. Schmid, M., and C.N. Toepfer. 2021. Cardiac myosin super relaxation (SRX): a perspective on fundamental biology, human disease and therapeutics. *Biol. Open*. 10:bio057646.

22. Kampourakis, T., Y.-B. Sun, and M. Irving. 2016. Myosin light chain phosphorylation enhances contraction of heart muscle via structural changes in both thick and thin filaments. *Proc National Acad Sci*. 113:E3039–E3047.

23. Kensler, R.W., R. Craig, and R.L. Moss. 2017. Phosphorylation of cardiac myosin binding protein C releases myosin heads from the surface of cardiac thick filaments. *Proc. Natl. Acad. Sci.* 114:E1355–E1364.

24. Ponnam, S., I. Sevrieva, Y.-B. Sun, M. Irving, and T. Kampourakis. 2019. Site-specific phosphorylation of myosin binding protein-C coordinates thin and thick filament activation in cardiac muscle. *Proc. Natl. Acad. Sci.* 116:15485–15494.

25. Fusi, L., E. Brunello, Z. Yan, and M. Irving. 2016. Thick filament mechano-sensing is a calcium-independent regulatory mechanism in skeletal muscle. *Nat. Commun.* 7:13281.

26. Caremani, M., E. Brunello, M. Linari, L. Fusi, T.C. Irving, D. Gore, G. Piazzesi, M. Irving, V. Lombardi, and M. Reconditi. 2019. Low temperature traps myosin motors of mammalian muscle in a refractory state that prevents activation. *J. Gen. Physiol.* 151:1272–1286.

27. Regnier, M., D.M. Lee, and E. Homsher. 1998. ATP Analogs and Muscle Contraction: Mechanics and Kinetics of Nucleoside Triphosphate Binding and Hydrolysis. *Biophys J.* 74:3044–3058.

28. Regnier, M., D.A. Martyn, and P.B. Chase. 1998. Calcium Regulation of Tension Redevelopment Kinetics with 2-Deoxy-ATP or Low [ATP] in Rabbit Skeletal Muscle. *Biophys J.* 74:2005–2015.

29. Regnier, M., H. Martin, R.J. Barsotti, A.J. Rivera, D.A. Martyn, and E. Clemmens. 2004. Cross-Bridge versus Thin Filament Contributions to the Level and Rate of Force Development in Cardiac Muscle. *Biophys J.* 87:1815–1824.

30. Regnier, M., A.J. Rivera, Y. Chen, and P.B. Chase. 2000. 2-Deoxy-ATP Enhances Contractility of Rat Cardiac Muscle. *Circ Res.* 86:1211–1217.

31. Ma, W., T.S. McMillen, M.C. Childers, H. Gong, M. Regnier, and T. Irving. 2023. Structural OFF/ON transitions of myosin in relaxed porcine myocardium predict calcium-activated force. *Proc National Acad Sci.* 120:e2207615120.

32. Powers, J.D., C.-C. Yuan, K.J. McCabe, J.D. Murray, M.C. Childers, G.V. Flint, F. Moussavi-Harami, S. Mohran, R. Castillo, C. Zuzek, W. Ma, V. Daggett, A.D. McCulloch, T.C. Irving, and M. Regnier. 2019. Cardiac myosin activation with 2-deoxy-ATP via increased electrostatic interactions with actin. *P Natl Acad Sci Usa.* 116:11502–11507.

33. Nowakowski, S.G., S.C. Kolwicz, F.S. Korte, Z. Luo, J.N. Robinson-Hamm, J.L. Page, F. Brozovich, R.S. Weiss, R. Tian, C.E. Murry, and M. Regnier. 2013. Transgenic overexpression of ribonucleotide reductase improves cardiac performance. *Proc. Natl. Acad. Sci.* 110:6187–6192.

34. Thomson, K.S., G.L. Odom, C.E. Murry, G.G. Mahairas, F. Moussavi-Harami, S.L. Teichman, X. Chen, S.D. Hauschka, J.S. Chamberlain, and M. Regnier. 2016. Translation of Cardiac Myosin Activation With 2-Deoxy-ATP to Treat Heart Failure Via an Experimental Ribonucleotide Reductase-Based Gene Therapy. *JACC: Basic Transl. Sci.* 1:666–679.

35. Kolwicz, S.C., G.L. Odom, S.G. Nowakowski, F. Moussavi-Harami, X. Chen, H. Reinecke, S.D. Hauschka, C.E. Murry, G.G. Mahairas, and M. Regnier. 2015. AAV6-mediated Cardiac-specific Overexpression of Ribonucleotide Reductase Enhances Myocardial Contractility. *Mol Ther J Am Soc Gene Ther.* 24:240–50.

36. Kolwicz, S.C., J.K. Hall, F. Moussavi-Harami, X. Chen, S.D. Hauschka, J.S. Chamberlain, M. Regnier, and G.L. Odom. 2019. Gene Therapy Rescues Cardiac Dysfunction in Duchenne Muscular Dystrophy Mice by Elevating Cardiomyocyte Deoxy-Adenosine Triphosphate. *JACC: Basic Transl. Sci.* 4:778–791.

37. Kadota, S., J. Carey, H. Reinecke, J. Leggett, S. Teichman, M.A. Laflamme, C.E. Murry, M. Regnier, and G.G. Mahairas. 2015. Ribonucleotide reductase-mediated increase in dATP improves cardiac performance via myosin activation in a large animal model of heart failure. *Eur J Heart Fail.* 17:772–81.

38. Cheng, Y., K.A. Hogarth, M.L. O'Sullivan, M. Regnier, and W.G. Pyle. 2016. 2-Deoxyadenosine triphosphate restores the contractile function of cardiac myofibril from adult dogs with naturally occurring dilated cardiomyopathy. *Am. J. Physiol.-Hear. Circ. Physiol.* 310:H80–H91.

39. Hu, Z., D.W. Taylor, M.K. Reedy, R.J. Edwards, and K.A. Taylor. 2016. Structure of myosin filaments from relaxed Lethocerus flight muscle by cryo-EM at 6 Å resolution. *Sci. Adv.* 2:e1600058.

40. Yang, S., P. Tiwari, K.H. Lee, O. Sato, M. Ikebe, R. Padrón, and R. Craig. 2020. Cryo-EM structure of the inhibited (10S) form of myosin II. *Nature.* 588:521–525.

41. AL-Khayat, H.A., R.W. Kensler, J.M. Squire, S.B. Marston, and E.P. Morris. 2013. Atomic model of the human cardiac muscle myosin filament. *Proc. Natl. Acad. Sci.* 110:318–323.

42. Woodhead, J.L., and R. Craig. 2019. The mesa trail and the interacting heads motif of myosin II. *Arch Biochem Biophys.* 680:108228.

43. McMillan, S.N., and C.A. Scarff. 2022. Cryo-electron microscopy analysis of myosin at work and at rest. *Curr Opin Struc Biol.* 75:102391.

44. Grinzato, A., D. Auguin, C. Kikuti, N. Nandwani, D. Moussaoui, D. Pathak, E. Kandiah, K.M. Ruppel, J.A. Spudich, A. Houdusse, and J. Robert-Paganin. 2023. Cryo-EM structure of the folded-back state of human β-cardiac myosin. *Nat Commun.* 14:3166.

45. Dutta, D., V. Nguyen, K.S. Campbell, R. Padrón, and R. Craig. 2023. Cryo-EM structure of the human cardiac myosin filament. *Nature.* 623:853–862.

46. Tamborrini, D., Z. Wang, T. Wagner, S. Tacke, M. Stabrin, M. Grange, A.L. Kho, M. Rees, P. Bennett, M. Gautel, and S. Raunser. 2023. Structure of the native myosin filament in the relaxed cardiac sarcomere. *Nature.* 623:863–871.

47. Shaw, D.E., J.P. Grossman, J.A. Bank, B. Batson, J.A. Butts, J.C. Chao, M.M. Deneroff, R.O. Dror, A. Even, C.H. Fenton, A. Forte, J. Gagliardo, G. Gill, B. Greskamp, C.R. Ho, D.J. Ierardi, L. Iserovich, J.S. Kuskin, R.H. Larson, T. Layman, L.-S. Lee, A.K. Lerer, C. Li, D. Killebrew, K.M. Mackenzie, S.Y.-H. Mok, M.A. Moraes, R. Mueller, L.J. Nociolo, J.L.

Peticolas, T. Quan, D. Ramot, J.K. Salmon, D.P. Scarpazza, U.B. Schafer, N. Siddique, C.W. Snyder, J. Spengler, P.T.P. Tang, M. Theobald, H. Toma, B. Towles, B. Vitale, S.C. Wang, and C. Young. 2014. Anton 2: Raising the Bar for Performance and Programmability in a Special-Purpose Molecular Dynamics Supercomputer. *SC14: Int. Conf. High Perform. Comput., Netw., Storage Anal.* 41–53.

48. Childers, M.C., M. Geeves, V. Daggett, and M. Regnier. 2021. Modulation of post-powerstroke dynamics in myosin II by 2′-deoxy-ADP. *Arch Biochem Biophys*. 699:108733.

49. Nowakowski, S.G., M. Regnier, and V. Daggett. 2017. Molecular mechanisms underlying deoxy-ADP.Pi activation of pre-powerstroke myosin. *Protein Sci Publ Protein Soc*. 26:749–762.

50. Andreani, R., J.M. Martínez, L. Martínez, and F. Yano. 2008. Continuous optimization methods for structure alignments. *Math. Program.* 112:93–124.

51. Martínez, L., R. Andreani, and J.M. Martínez. 2007. Convergent algorithms for protein structural alignment. *BMC Bioinform.* 8:306.

52. Martínez, L. 2015. Automatic Identification of Mobile and Rigid Substructures in Molecular Dynamics Simulations and Fractional Structural Fluctuation Analysis. *PLoS ONE*. 10:e0119264.

53. Martin, J., and E. Frezza. 2022. A dynamical view of protein-protein complexes: Studies by molecular dynamics simulations. *Front. Mol. Biosci.* 9:970109.

54. Childers, M.C., and V. Daggett. 2018. Validating Molecular Dynamics Simulations against Experimental Observables in Light of Underlying Conformational Ensembles. *J Phys Chem B*. 122:6673–6689.

55. Sawle, L., and K. Ghosh. 2016. Convergence of Molecular Dynamics Simulation of Protein Native States: Feasibility vs Self-Consistency Dilemma. *J Chem Theory Comput*. 12:861–9.

56. Ma, W., M. Childers, J. Murray, F. Moussavi-Harami, H. Gong, R. Weiss, V. Daggett, T. Irving, and M. Regnier. 2020. Myosin dynamics during relaxation in mouse soleus muscle and modulation by 2′-deoxy-ATP. *J Physiology*. 598:5165–5182.

57. Spudich, J.A., N. Nandwani, J. Robert-Paganin, A. Houdusse, and K.M. Ruppel. 2024. Reassessing the unifying hypothesis for hypercontractility caused by myosin mutations in hypertrophic cardiomyopathy. EMBO J. 1–17.

58. Auguin, D., J. Robert-Paganin, S. Réty, C. Kikuti, A. David, G. Theumer, A.W. Schmidt, H.-J. Knölker, and A. Houdusse. 2023. Omecamtiv mecarbil and Mavacamten target the same

myosin pocket despite antagonistic effects in heart contraction. *bioRxiv*. 2023.11.15.567213.

59. Robert-Paganin, J., D. Auguin, and A. Houdusse. 2018. Hypertrophic cardiomyopathy disease results from disparate impairments of cardiac myosin function and auto-inhibition. *Nat Commun*. 9:4019.

60. Alamo, L., D. Qi, W. Wriggers, A. Pinto, J. Zhu, A. Bilbao, R.E. Gillilan, S. Hu, and R. Padrón. 2016. Conserved Intramolecular Interactions Maintain Myosin Interacting-Heads Motifs Explaining Tarantula Muscle Super-Relaxed State Structural Basis. *J Mol Biol*. 428:1142–1164.

61. Homburger, J.R., E.M. Green, C. Caleshu, M.S. Sunitha, R.E. Taylor, K.M. Ruppel, R.P.R. Metpally, S.D. Colan, M. Michels, S.M. Day, I. Olivotto, C.D. Bustamante, F.E. Dewey, C.Y. Ho, J.A. Spudich, and E.A. Ashley. 2016. Multidimensional structure-function relationships in human β-cardiac myosin from population-scale genetic variation. *Proc National Acad Sci*. 113:6701–6706.

62. Wells, C., and C.R. Bagshaw. 1985. Calcium regulation of molluscan myosin ATPase in the absence of actin. *Nature*. 313:696–697.

63. Pilagov, M., L.W.H.J. Heling, J. Walklate, M.A. Geeves, and N.M. Kad. 2022. Single-molecule imaging reveals how mavacamten and PKA modulate ATP turnover in skeletal muscle myofibrils. *J. Gen. Physiol.* 155:e202213087.

64. Bennett, P., M. Rees, and M. Gautel. 2020. The Axial Alignment of Titin on the Muscle Thick Filament Supports Its Role as a Molecular Ruler. *J. Mol. Biol.* 432:4815–4829.